ZH production in gluon fusion at NLO in QCD

Long Chen,[a,i] **Joshua Davies,**[b] **Gudrun Heinrich,**[c] **Stephen P. Jones,**[d]
Matthias Kerner,[c,e] **Go Mishima,**[f] **Johannes Schlenk**[g] **and Matthias Steinhauser**[h]

[a]*Institute for Theoretical Particle Physics and Cosmology, RWTH Aachen University,*
52056 Aachen, Germany

[b]*Department of Physics and Astronomy, University of Sussex,*
Brighton BN1 9QH, U.K.

[c]*Institute for Theoretical Physics, Karlsruhe Institute of Technology,*
76128 Karlsruhe, Germany

[d]*Institute for Particle Physics Phenomenology, Durham University,*
Durham DH1 3LE, U.K.

[e]*Institute for Astroparticle Physics, Karlsruhe Institute of Technology,*
76344 Eggenstein-Leopoldshafen, Germany

[f]*Department of Physics, Tohoku University,*
Sendai, 980-8578 Japan

[g]*Theory Group LTP, Paul Scherrer Institut,*
CH-5232 Villigen PSI, Switzerland

[h]*Institute for Theoretical Particle Physics, Karlsruhe Institute of Technology,*
76128 Karlsruhe, Germany

[i]*School of Physics, Shandong University,*
Jinan, Shandong 250100, China

E-mail: longchen@physik.rwth-aachen.de, j.o.davies@sussex.ac.uk,
gudrun.heinrich@kit.edu, s.jones@cern.ch, matthias.kerner@kit.edu,
go.mishima@icloud.com, johannes.schlenk@psi.ch,
matthias.steinhauser@kit.edu

ABSTRACT: We present fully differential next-to-leading order results for Higgs production in association with a *Z* boson in gluon fusion. Our two-loop virtual contributions are evaluated numerically using sector decomposition, including full top-quark mass effects, and supplemented at high p_T by an analytic high-energy expansion to order (m_Z^4, m_H^4, m_t^{32}). Using the expanded results we also present a study of the top-quark mass scheme uncertainty at large p_T.

Contents

1 Introduction

Higgs boson production in association with a Z boson is a particularly interesting process as it probes both the Higgs boson coupling to Z bosons as well as to fermions. Despite its relatively small cross section, the process $pp \to ZH$ in combination with the decay channel $H \to b\bar{b}$ was the "discovery channel" for Higgs boson couplings to bottom quarks [1, 2], as while inclusive $H \to b\bar{b}$ suffers from large backgrounds, the Z boson offers straightforward triggering. Recently, associated Higgs production was also used to place limits on the Higgs-charm coupling [3, 4].

The loop-induced gluon channel formally enters at next-to-next-to-leading order (NNLO), with respect to the $pp \to ZH$ process. However, due to the dominance of the gluon parton distribution function (PDF) at the LHC, this channel is sizeable; it contributes about 6% to the total NNLO cross section and becomes significant in the boosted Higgs regime for $p_T^H \gtrsim 150\,\mathrm{GeV}$ [5–9]. For more details about calculations of higher-order corrections to the $pp \to ZH$ process we refer to ref. [10]; here we focus on the gluon channel.

Experimental measurements of ZH production [11–17] still suffer from large statistical uncertainties, however the statistics will improve considerably in LHC Run 3 and at the High Luminosity LHC. On the theoretical side, the scale uncertainties for this process are large. They are dominated by the $gg \to ZH$ channel which, being loop induced, enters at its leading order (LO) into the simulation programs [18–25] used by the experimental collaborations. Therefore next-to-leading order (NLO) QCD corrections to the $gg \to ZH$ process, calculated at LO in ref. [26], are important; particularly so in view of providing constraints on anomalous couplings, because of the sensitivity of this process to both the Higgs couplings to fermions as well as to vector bosons. Furthermore, it provides a way

to put constraints on the sign of the top quark Yukawa coupling as well as on its CP structure [7, 20, 21, 27, 28], because the cross section has a component where this coupling enters linearly. Recently, it was shown [29] that this process also has the potential to probe anomalous $Zb\bar{b}$ couplings and thus to shed light on the long-standing discrepancy of the forward-backward asymmetry A^b_{FB} measured at LEP, with the Standard Model prediction.

The NLO QCD two-loop amplitude for $gg \to ZH$, including full top-quark mass effects, has been calculated numerically in ref. [30]. The two-loop amplitude has also been calculated based on high-energy (also sometimes called "small-mass") and large-m_t expansions, supplemented with Padé approximants to improve the description beyond the high-energy radius of convergence [31]. Results for the virtual corrections based on a transverse-momentum expansion are also available [32]. Recently, the virtual corrections to both $gg \to HH$ and $gg \to ZH$, based on a combination of transverse-momentum expansion and high-energy expansion, have been presented in ref. [33]. The total cross section and invariant-mass distribution for $gg \to ZH$ at NLO QCD has been calculated in ref. [34], based on a small-(m_Z, m_H) expansion [35] of the two-loop amplitude, retaining the full top-quark mass dependence. An expansion of the virtual and real NLO contributions to $gg \to ZH$ for large m_t has been computed in [36].

In this work we present full NLO QCD results for the $gg \to ZH$ process where the two-loop amplitude is based on a combination of the numerical results of ref. [30] and an extended version of the results from the high-energy expansion of ref. [31], thereby providing reliable and accurate results in all kinematic regions, in particular in the boosted Higgs regime which is particularly sensitive to new physics effects. A similar combination has already been carried out successfully for Higgs boson pair production [37]. In addition, we consider two renormalisation schemes for the top quark mass, the on-shell (OS) scheme and the modified Minimal Subtraction ($\overline{\text{MS}}$) scheme, and investigate how the scheme dependence impacts the phenomenological results.

This paper is organised as follows. In section 2 we describe the calculation of the NLO corrections and the combination procedure. Section 3 contains results for the total cross section at different center-of-mass energies as well as ZH invariant-mass and transverse-momentum distributions. The second part of section 3 is dedicated to the discussion of the top-quark mass scheme dependence, before we conclude in section 4.

2 Setup of the calculation

In this section we summarise the computation of the individual contributions to the cross section at NLO and describe the combination of the virtual corrections computed in [31] and [30].

2.1 Virtual two-loop contributions

The calculation of the renormalised and infrared (IR) subtracted two-loop amplitude, called $\mathcal{V}$, is described in detail in refs. [31] and [30]. For completeness we repeat in the following the most important steps.
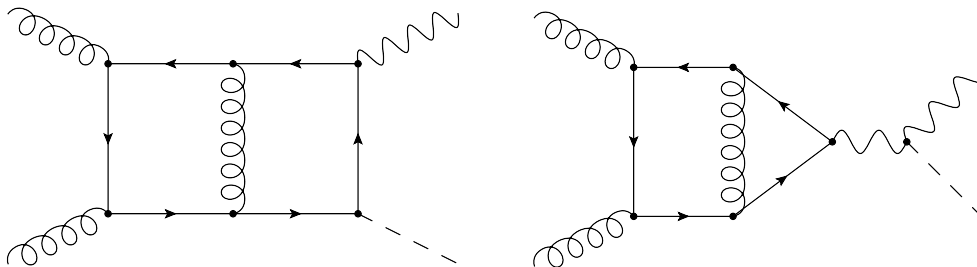
Figure 1. Representative Feynman diagrams for the virtual correction to the *ggZH* amplitude. We neglect the masses of all quarks except the top quark; therefore, due to the Yukawa couplings, only the top quark gives a non-zero contribution for the box diagrams. All quark flavours contribute for the triangle diagrams, however the contribution from each massless generation is zero due to a cancellation between the up-type and down-type quarks. We calculate in the Feynman gauge and so also include the set of diagrams where the *Z*-boson propagators are replaced by Goldstone bosons.

In ref. [31] the amplitude of the process $gg \to ZH$ has been written as a linear combination of six form factors. At one-loop order it is straightforward to obtain exact results for the form factors. At two-loops expansions for large and small top-quark masses were performed. In this work only the high-energy expansion, for which $m_H^2, m_Z^2 \ll m_t^2 \ll s, |t|$, is of relevance. In ref. [31] an expansion up to order (m_Z^2, m_H^2, m_t^{32}) was computed. In this work we extend that result up to quartic order (m_Z^4, m_H^4, m_t^{32}) (including also the "mixed" quartic term $m_Z^2 m_H^2$) and show that including these quartic terms improves the agreement with numerical results. LiteRed [38] is used to expand the integrals appearing in the amplitude, followed by an integration-by-parts (IBP) reduction to master integrals using FIRE [39]. The reduction relations are substituted into the amplitude and simplified using FORM [40]. In ref. [31] it was shown that Padé approximants for the expansion in m_t significantly improve the description beyond the radius of convergence of the naive expansion and reliable results can be obtained for $p_T \geq 150\,\text{GeV}$ (see figure 2); we apply the same procedure here. Note that in this approach one can construct the high-energy expansion of $\mathcal{V}$ as a function of m_H, m_Z and m_t which allows for a variation of these parameters. Furthermore, it is straightforward to perform a scheme change and convert the top quark mass from the OS to the $\overline{\text{MS}}$ scheme. The subsequent construction of the new Padé approximants requires only negligible CPU time.

In ref. [30], the two-loop amplitudes have been calculated via a projection onto a basis of linear polarisation states as suggested in ref. [41]. For the IBP reduction of the resulting form factors to master integrals we used Kira [42–44] in combination with the rational function interpolation library FireFly [45, 46]. For the numerical integration, using a quasi-finite basis [47] of master integrals is beneficial. This basis is related to the default basis by dimension shifts and higher powers of propagators (dots). For the derivation of the set of dimensional recurrence relations which connects integrals in $D + 2n$ and D dimensions, we used LiteRed [38] and Reduze [48].

To evaluate the master integrals, we applied sector decomposition as implemented in the program pySecDec [49, 50], using a quasi-Monte Carlo algorithm [50, 51] for the nu-

merical integration. In particular, we made use of one of the new features of `pySecDec` [52] to integrate a weighted sum of integrals such that the number of sampling points used for each integral is dynamically set, according to its contribution to the total uncertainty of the amplitude.

We renormalise the strong coupling in the $\overline{\text{MS}}$ scheme with 5 active quark flavours. The top quark mass is renormalised in either the OS scheme or the $\overline{\text{MS}}$ scheme, as indicated. Expanding each renormalised form factor $\mathcal{A}_{i=1,\dots,n}$ in powers of the strong coupling, $a_s = \alpha_s/(4\pi)$, we may write

$$\mathcal{A}_i^{\text{UV}} = a_s A_i^{(0),\text{UV}} + a_s^2 A_i^{(1),\text{UV}} + \mathcal{O}(a_s^3) \tag{2.1}$$

and then obtain IR-finite amplitudes using the Catani-Seymour subtraction operator [53]

$$A_i^{(0),\text{fin}} = A_i^{(0),\text{UV}}, \tag{2.2}$$

$$A_i^{(1),\text{fin}} = A_i^{(1),\text{UV}} - I_1 A_i^{(0),\text{UV}}. \tag{2.3}$$

The squared $2 \to 2$ amplitude, in the helicity basis, can be written as

$$\overline{\sum} |A_i^{\text{fin}}|^2 = a_s^2 \mathcal{B} + a_s^3 \mathcal{V} + \mathcal{O}(a_s^4), \tag{2.4}$$

where the squared Born amplitude ($\mathcal{B}$) and the Born-virtual interference ($\mathcal{V}$), are given by

$$\mathcal{B} = \overline{\sum} A_i^{(0),\text{fin}} A_i^{*(0),\text{fin}}, \tag{2.5}$$

$$\mathcal{V} = \overline{\sum} \left(A_i^{(0),\text{fin}} A_i^{*(1),\text{fin}} + A_i^{(1),\text{fin}} A_i^{*(0),\text{fin}} \right). \tag{2.6}$$

The sum/average, denoted by $\overline{\sum}$, runs over all helicities and averages over the incoming spin and colour indices.

2.1.1 Combination of the two approaches

In figure 2 we show the difference between the two calculations of the two-loop virtual amplitudes, relative to the LO amplitude. This difference is independent of the IR subtraction scheme used for removing the IR singularities. The plot shows that the Padé-improved high-energy expansion converges on the full result for $p_T \gtrsim 150\,\text{GeV}$. However, using only the quadratic terms in m_Z^2 and m_H^2 in the expansion, a difference at the two permille level remains even at large p_T. After including the quartic terms in the expansion, most of the points with $p_T > 200\,\text{GeV}$ agree within the numerical uncertainty at the $2 \cdot 10^{-5}$ level (with a few outliers with large numerical uncertainty reaching up to the $2 \cdot 10^{-3}$ level). At low p_T the differences increase, reaching up to 0.15% at $200\,\text{GeV}$ and up to 2.8% at $150\,\text{GeV}$.

Since the two results are consistent for sufficiently large p_T, in section 3.1 we combine the two approaches and we use the results based on the high-energy expansion for contributions with $p_T > 200\,\text{GeV}$ and use the numerical evaluation of the amplitude only for $p_T < 200\,\text{GeV}$. The two contributions are then combined at the histogram level. Our results are therefore valid in all phase-space regions, but avoid the costly numerical evaluation in large parts of the phase space. For the study of the top quark mass renormalization scheme dependence in section 3.2, the high-energy expansion is used for all results (i.e. $p_T > 150\,\text{GeV}$), since in the numerical calculation, the top-quark mass was fixed during the reduction.
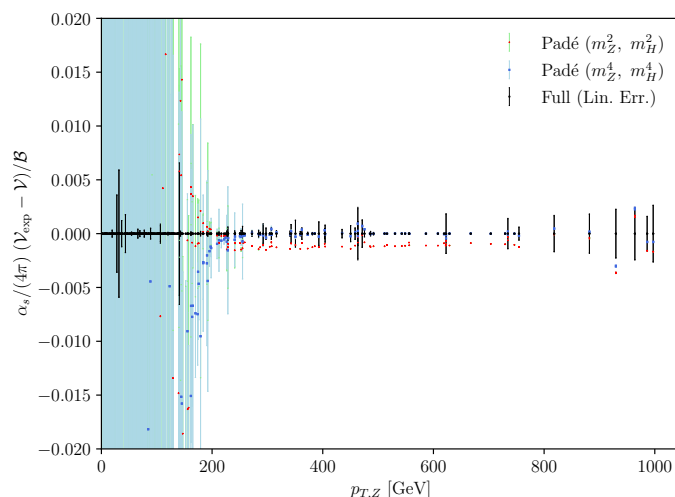
Figure 2. Comparison of the full and Padé improved high-energy expanded results normalised to the Born result, as a function of $p_{T,Z}$. The Padé-improved results are shown including up to quadratic terms, $(m_Z^2,\ m_H^2)$, or quartic terms, $(m_Z^4,\ m_H^4)$, in m_Z and m_H. For this comparison we fix the strong coupling constant to $\alpha_s = 0.118$.

2.1.2 Phase-space sampling

The integration of $\mathcal{V}$ over the phase space is achieved by a reweighting procedure based on the Born events. Specifically, we use the events of a LO calculation and apply the accept-reject method to obtain a list of sampling points for the virtual contribution distributed according to the probability density function $\sim \mathcal{L}_{gg,0}\, |\mathcal{B}_0|^2\, \frac{d\mathrm{PS}}{f(p_T,m_{ZH})}$, where $\mathcal{L}_{gg,0}$ is the gluon-gluon luminosity as defined in ref. [54] and $\mathcal{B}_0$ is the LO matrix element as used in the LO calculation. The factor $d\mathrm{PS}$ is the Jacobian of the phase-space integration and the function $f(p_T, m_{ZH})$ can be used to enhance the number of sampling points in specific regions. Choosing, e.g., $f = f(m_{ZH}) \propto \mathrm{d}\sigma_B/\mathrm{d}m_{ZH}$ leads to sampling points which are uniformly distributed in m_{ZH}, thus enhancing the number of events in the tail of the distribution, whereas $f(p_T, m_{ZH}) = 1$ results in sampling points distributed according to the fully differential LO cross section.

The virtual contribution to the cross section is then given by

$$\sigma_V = \frac{1}{N} \sum_{\mathrm{N\ sampling\ points}} \frac{\mathcal{L}_{gg}\, \mathcal{V}}{\mathcal{L}_{gg,0}\, |\mathcal{B}_0|^2} \cdot f(p_T, m_{ZH})\, \sigma_{B,0}, \tag{2.7}$$

where $\mathcal{L}_{gg}$ and $\mathcal{V}$ are the new gluon-gluon luminosity and virtual matrix elements, whereas $\mathcal{L}_{gg,0}$, $\mathcal{B}_0$ and $\sigma_{B,0}$ are obtained from the original LO calculation, with the total LO cross section $\sigma_{B,0}$.

In the following results we use three different sets of sampling points, optimized for the total cross section, as well as the m_{ZH} and p_T distributions. While the exact form of $f(p_T, m_{ZH})$ is not important, a good choice can be obtained with a fit using a Padé ansatz. In the region $p_T, m_{ZH} \geq 2\,\mathrm{TeV}$, where a uniform sampling of points is not needed, we keep f constant. In total, we use 1294 numerically evaluated points distributed according to
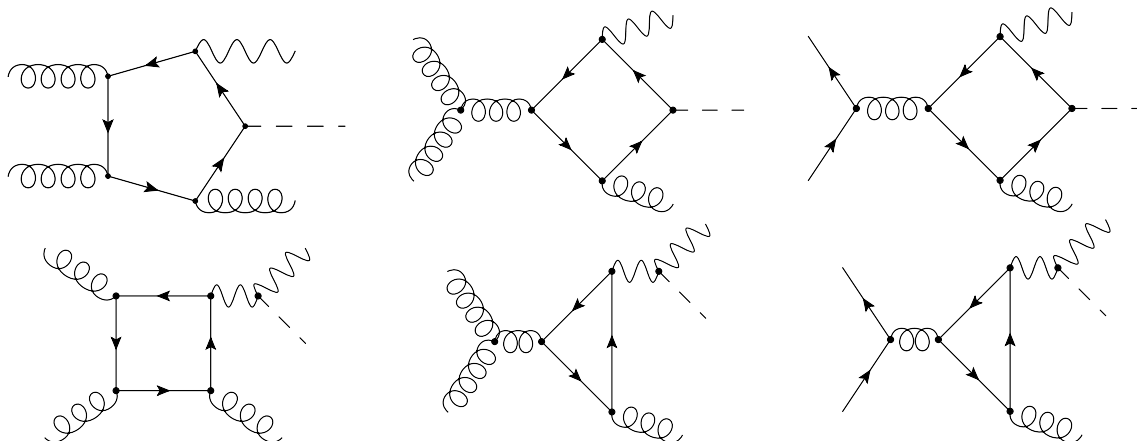
Figure 3. Representative Feynman diagrams for the real correction amplitudes $ggZHg$ and $q\bar{q}ZHg$, with $n_f = 5$ massless quarks and a massive top quark running in the closed fermion loops. We calculate in the Feynman gauge and so also include the set of diagrams in which the Z-boson propagators are replaced by Goldstone bosons.
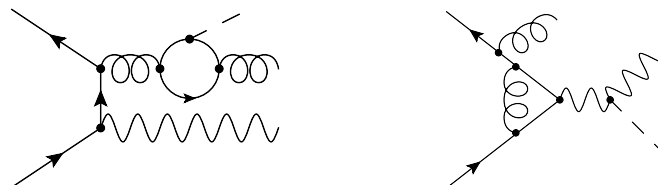

Figure 4. Representative Feynman diagrams for the class of real corrections excluded in this work; we exclude diagrams in which the Z boson couples to the external quark line.

the differential LO cross section. For the m_{ZH} and p_T distributions, we combine these results with sets containing an additional 6000 points, optimised for the corresponding distribution, evaluated using the Padé-improved high-energy expansion.

2.2 Computation of the real radiation contributions

The real radiation matrix elements are calculated using the one-loop amplitude generator GoSam [55, 56] together with an in-house C++ code, similar to the one used in refs. [54, 57], where the IR singularities are subtracted in the Catani-Seymour scheme [53], supplemented by a dipole phase-space cut parameter α_{cut} [58]. We have checked that our implementation of the dipoles reproduces the matrix element in the soft and collinear limits and that our results are independent of α_{cut} for $0.2 \leq \alpha_{\text{cut}} \leq 1$.

To check the numerical precision of our real matrix elements we use several rotation tests (i.e., we perform azimuthal rotations about the beam axis and recompute the phase-space point). We first compute the matrix element at a given phase-space point and a rotated phase-space point in double precision. If the results do not agree to 10 digits, we compute the phase-space point in quadruple precision and check if it agrees with the double-precision evaluations to 7 digits. If the results do not agree we compute a rotated point in quadruple precision and check that the quadruple-precision results agree to 10 digits; a

vanishingly small fraction of points failed this test and were discarded. Using the above procedure, we did not find it necessary to apply a technical cut to our $2 \to 3$ phase space.

In figure 3 we show examples of the Feynman diagrams included in our real radiation. We include all diagrams appearing in the $ggZHg$ and $q\bar{q}ZHg$ amplitudes (as well as their crossings) which contain a closed fermion loop and have either a Z-boson or Goldstone boson coupled to that loop. We consider $n_f = 5$ massless quarks and a massive top quark running in the fermion loops. Due to the presence of the Yukawa coupling in the upper diagrams, the massless quarks give a non-zero contribution only for the lower row of diagrams. For the diagrams in the second and third column of the lower row, the contribution of each massless generation is zero due to a cancellation between the up-type and down-type quarks. We calculate in the Feynman gauge and so also include the set of diagrams in which the Z-boson propagators are replaced by Goldstone bosons.

In figure 4 we show examples of Feynman diagrams which are not included in this work; these diagrams do not have a Z boson or Goldstone boson coupled to the closed fermion loop and so belong to the Drell-Yan class of diagrams, which we do not consider. The class of diagrams with the Higgs boson coupled to a closed quark loop, represented by the left figure, is UV/IR finite and separately gauge invariant; it was considered in detail in ref. [59].

3 Results

3.1 Total and differential cross sections

Our results are based on a center-of-mass energy of $\sqrt{s} = 14\,\text{TeV}$ unless stated otherwise. We use the NNPDF31_nlo_pdfas parton distribution functions [60] with masses determined by the ratios $m_Z^2/m_t^2 = 23/83$ and $m_H^2/m_t^2 = 12/23$ with $m_t = 173.21\,\text{GeV}$ and $m_W = 80.379\,\text{GeV}$, to 4 significant figures these ratios yield $m_Z = 91.18\,\text{GeV}$ and $m_H = 125.1\,\text{GeV}$.

Results for the total cross section with full top-quark mass dependence at three different center-of-mass energies, including scale uncertainties resulting from the 7-point scale variation, $\mu_{R,F} = \xi_{R,F}\, m_{ZH}$ with $\xi_{R,F} = (2,2),(2,1),(1,2),(1,1),(1,\frac{1}{2}),(\frac{1}{2},1),(\frac{1}{2},\frac{1}{2})$, are shown in table 1. Our result for $\sqrt{s} = 13\,\text{TeV}$ can be compared with that of ref. [34], where the virtual amplitude is computed in an expansion around small-m_Z and m_H, retaining the full m_t dependence. At Born level, we observe that their result is 2.7% larger than ours; we have verified that this is due only to the different choice of PDFs and masses (m_Z, m_H and m_t). At NLO their result is 2% larger than ours, we ascribe this difference again to the different choice of PDFs and masses. In ref. [34] the scale uncertainty is assessed via a 3-point scale variation by a factor of 3; adopting this procedure we agree with their scale uncertainty of $^{+27\%}_{-21\%}$ at NLO.

Differential results for the invariant mass $m_{ZH} = (p_Z + p_H)^2$ of the Z-Higgs system are shown in figure 5 for the central scale choices m_{ZH} and H_T, with

$$H_T = \sum_{i=H,Z} \sqrt{m_i^2 + p_{T,i}^2} + \sum_k |p_{T,k}|, \tag{3.1}$$

$\sqrt{s}$	LO [fb]	NLO [fb]
13 TeV	$52.42^{+25.5\%}_{-19.3\%}$	$103.8(3)^{+16.4\%}_{-13.9\%}$
13.6 TeV	$58.06^{+25.1\%}_{-19.0\%}$	$114.7(3)^{+16.2\%}_{-13.7\%}$
14 TeV	$61.96^{+24.9\%}_{-18.9\%}$	$122.2(3)^{+16.1\%}_{-13.6\%}$

Table 1. Total cross sections at LO and NLO with full top-quark mass dependence, evaluated at the scale $\mu_R = \mu_F = m_{ZH}$. The upper and lower values resulting from a 7-point scale variation by a factor of two are also shown.
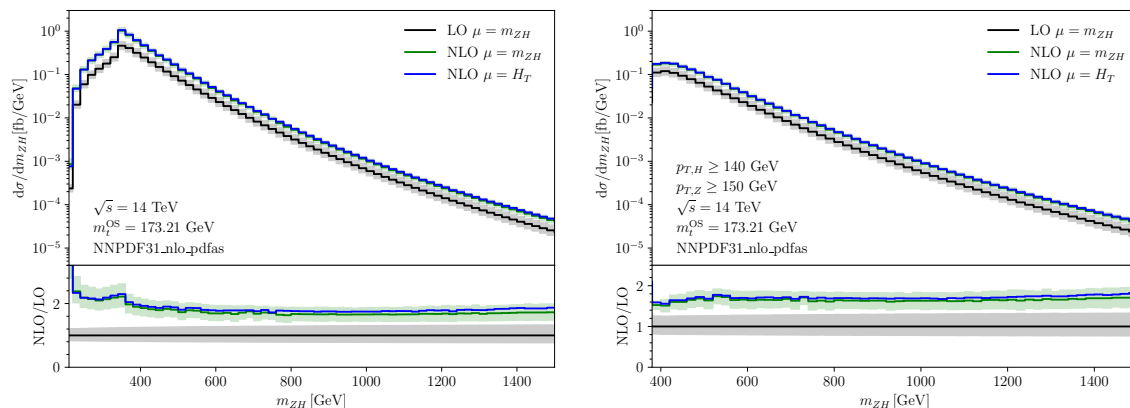

Figure 5. Invariant mass distribution at LO and NLO, including scale uncertainties resulting from a 7-point scale variation around the central scale $\mu = \mu_R = \mu_F = m_{ZH}$. We also show NLO predictions for $\mu = H_T$. Left: fully inclusive, right: results based on $p_{T,H} \geq 140\,\text{GeV}$, $p_{T,Z} \geq 150\,\text{GeV}$.

where the sum runs over all final state massless partons k. For the fully-inclusive case (left), the K-factor is relatively flat with a value of about two, except at very low invariant masses where threshold corrections are significant. The kink in the distribution at $m_{ZH} \simeq 350\,\text{GeV}$ is related to the $t\bar{t}$-production threshold. Only a small reduction of the scale uncertainty is observed going from LO to NLO. Note that the quark-gluon channel for this process first opens up at the NLO level. The cuts $p_{T,H} \geq 140\,\text{GeV}$, $p_{T,Z} \geq 150\,\text{GeV}$ (figure 5 (right)) somewhat decrease the K-factor.

The Z-boson transverse momentum distributions at LO and NLO are shown in figure 6. In the left plot we observe a K-factor which rises with increasing $p_{T,Z}$, reaching a value of almost 5 at $p_{T,Z} = 1\,\text{TeV}$, it is only slightly tamed by the cuts on $p_{T,H}$ and $p_{T,Z}$ (right plot).

Figure 7 shows the Higgs-boson transverse momentum distributions with and without p_T cuts. In the inclusive case (left) an extreme rise of the K-factor with increasing $p_{T,H}$, up to values of about 20 towards $p_{T,H} = 1\,\text{TeV}$, is observed. The cuts $p_{T,H} \geq 140\,\text{GeV}$, $p_{T,Z} \geq 150\,\text{GeV}$ decrease this K-factor by a factor of about 3 at large $p_{T,H}$ values. The cuts have such a large effect on the K-factor of this distribution as they remove configurations with a hard jet recoiling against a relatively hard Higgs while the Z boson is soft, this configuration dominates the tail of the distribution but is not present at LO. This behaviour was already
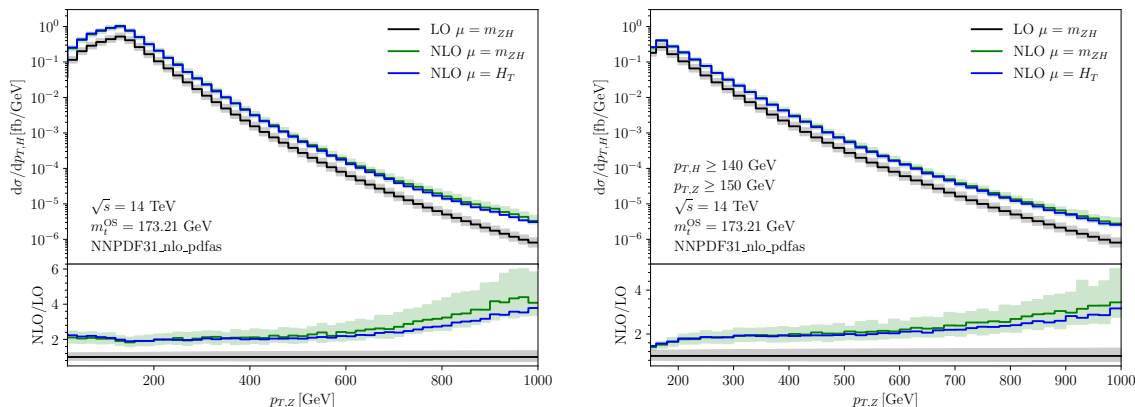
Figure 6. Distribution of the Z-boson transverse momenta at LO and NLO, including scale uncertainties resulting from a 7-point scale variation around the central scale $\mu = \mu_R = \mu_F = m_{ZH}$. We also show NLO predictions for $\mu = H_T$. Left: fully inclusive, right: results based on $p_{T,H} \geq 140\,\text{GeV}$, $p_{T,Z} \geq 150\,\text{GeV}$.
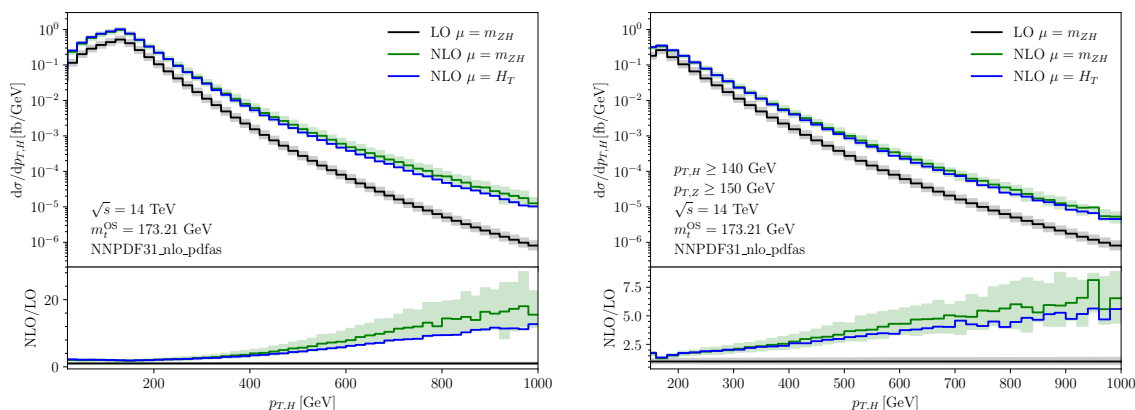

Figure 7. Higgs-boson transverse momentum distribution at LO and NLO, including scale uncertainties resulting from a 7-point scale variation around the central scale $\mu_R = \mu_F = m_{ZH}$. Left: fully inclusive, right: results based on $p_{T,H} \geq 140\,\text{GeV}$, $p_{T,Z} \geq 150\,\text{GeV}$.

reported in ref. [20] and traced back to diagrams with t-channel gluon exchange, it was further studied in ref. [61]. The reason why the rise of the K-factor is more pronounced in the $p_{T,H}$ case than in the $p_{T,Z}$ case can be related to the coupling structure of the Z and Higgs bosons to top quarks. In the diagrams where both the Higgs and the Z boson are radiated from a top quark loop, the probability to radiate a "soft" Z boson while the Higgs boson recoils against a hard jet is related to the soft Eikonal factor $p^\mu/(p \cdot p_Z)$, where p^μ generically denotes the radiator momentum. The probability to radiate a "soft" Higgs boson on the other hand is proportional to $m_t/(p \cdot p_H)$. The ratio of these Eikonal factors is $\simeq p_T/m_t \gg 1$, thus at large transverse momentum p_T of the radiator it is more likely that the Z boson is soft and the Higgs boson is hard.
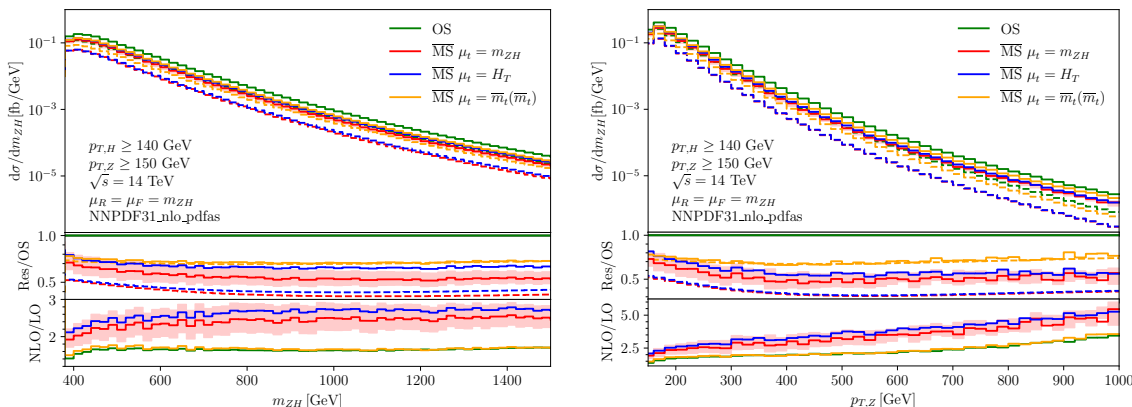
Figure 8. Comparison of differential results using various top quark mass schemes at LO (dashed) and NLO (solid). Left: invariant mass. Right: Z-boson transverse momentum.

3.2 Investigation of different top quark mass renormalisation schemes

We now turn to the discussion of the uncertainties stemming from the use of different top quark mass renormalisation schemes. Such uncertainties have been investigated in detail for the case of Higgs boson pair production in refs. [61–64]. For top quark pair production at NNLO, scheme uncertainties have been studied in ref. [65]. Top quark renormalisation scheme uncertainties also have been investigated for NLO $t\bar{t}H$ [66] and $t\bar{t}j$ [67] production at the LHC, as well as for off-shell Higgs production and LO Higgs+jet production [61].

In this section we investigate the top-quark mass renormalisation scheme dependence of ZH production. For this purpose we convert the top quark mass to the $\overline{\text{MS}}$ scheme, which is an appropriate renormalisation scheme in the high-energy region. It is thus sufficient to perform the scheme change in the analytic high-energy expansion of the virtual corrections, where it is straightforward to obtain the corresponding analytic expressions by making the replacement

$$m_t \; \rightarrow \; \overline{m}_t(\mu_t) \; \left(1 + \frac{\alpha_s(\mu_R)}{4\pi} C_F \left\{ 4 + 3 \log \left[\frac{\mu_t^2}{\overline{m}_t(\mu_t)^2} \right] \right\} \right) \tag{3.2}$$

and to apply the Padé procedure as described in section 2.1. Afterwards the result is combined with the real-radiation contributions where the $\overline{\text{MS}}$ top quark mass is used in the numerical evaluation.

We make three different choices for the central value of the top quark renormalisation scale, μ_t,

- $\mu_t = m_{ZH}$

- $\mu_t = H_T = \sum_{i=H,Z} \sqrt{m_i^2 + p_{T,i}^2} + \sum_k |p_{T,k}|$ (k sums over massless partons)

- $\mu_t = \overline{m}_t(\overline{m}_t)$

and vary μ_t up and down by a factor of 2 to obtain an uncertainty estimate.

For the conversion of the numerical values of the top quark mass between the OS and the $\overline{\text{MS}}$ schemes we proceed as follows: we first convert the top quark OS mass to the $\overline{\text{MS}}$

m_t Scheme	LO [fb/GeV]	NLO [fb/GeV]	LO: OS/Res	NLO: OS/Res
OS	$5.35 \cdot 10^{-4}$	$8.72(5) \cdot 10^{-4}$	1.0	1.0
$\overline{\text{MS}}\ (\mu_t = m_{ZH})$	$1.87 \cdot 10^{-4}$	$4.66(8) \cdot 10^{-4}$	2.85	1.87
$\overline{\text{MS}}\ (\mu_t = H_T)$	$2.10 \cdot 10^{-4}$	$5.69(8) \cdot 10^{-4}$	2.55	1.54
$\overline{\text{MS}}\ (\mu_t = \overline{m}_t(\overline{m}_t))$	$3.72 \cdot 10^{-4}$	$6.18(6) \cdot 10^{-4}$	1.44	1.41

Table 2. The LO and NLO results in various top quark mass schemes for $\sqrt{s} = 14$ TeV in the bin $m_{ZH} = [1000, 1020]$ GeV. The rightmost columns show the ratio of the on-shell result to results in other mass schemes at LO and NLO in this bin, respectively. Transverse momentum cuts of $p_{T,H} \geq 140$ GeV and $p_{T,Z} \geq 150$ GeV are applied and the remaining scales are set to $\mu_R = \mu_F = m_{ZH}$.

scheme at the scale $\mu_t = \overline{m}_t$, at four-loop accuracy. For our input values, $m_t = 173.21\,\text{GeV}$ and $\alpha_s(m_Z) = 0.118$, this gives $\overline{m}_t(\overline{m}_t) = 163.39\,\text{GeV}$. We then use the renormalisation group equation, at five-loop accuracy with six active quark flavours, to run from $\mu_t = \overline{m}_t$ to the desired renormalisation scale for $\overline{m}_t$. For both the numerical scheme conversion and the running we use the Mathematica and C++ codes RunDec and CRunDec [68, 69].

At LO the difference between the schemes is purely parametric and is driven both by the top quark mass appearing in the propagators and the Higgs-top Yukawa coupling. At NLO the OS and $\overline{\text{MS}}$ schemes differ by the parametric choice of m_t and a shift proportional to the derivative of the LO, i.e., the mass counterterms, which partly compensates the parametric difference.

In figure 8 we show predictions at LO (dashed lines) and NLO (solid lines) for $\mu_R = \mu_F = m_{ZH}$ with three different choices of the top-quark renormalisation scale, μ_t. The red band is generated by varying the scale $\mu_t = m_{ZH}$ up and down by a factor of 2, keeping $\mu_R = \mu_F = m_{ZH}$ fixed. We observe that the scheme choice for the top quark mass has a large impact on the predictions for both the invariant mass distribution (with $p_{T,H} \geq 140$ GeV and $p_{T,Z} \geq 150$ GeV cuts) and the $p_{T,Z}$ distribution. Focusing on the invariant mass distribution, we observe that at LO for $m_{ZH} \sim 1$ TeV the OS result is approximately a factor of 2.9 times the $\overline{\text{MS}}$ result with $\mu_t = m_{ZH}$. At NLO the difference between the schemes is somewhat reduced, with the OS result around 1.9 times the $\overline{\text{MS}}$ result with $\mu_t = m_{ZH}$, see table 2. Taking, for example, the difference between the OS and the $\overline{\text{MS}}$ result with $\mu_t = m_{ZH}$ as a mass scheme uncertainty would result in a $^{+0\%}_{-65\%}$ uncertainty at LO and a $^{+0\%}_{-47\%}$ uncertainty at NLO for $m_{ZH} = 1$ TeV. Alternatively, taking the $\overline{\text{MS}}$ result with $\mu_t = (m_{ZH}/2,\ m_{ZH},\ 2\,m_{ZH})$ as an uncertainty gives $^{+26\%}_{-21\%}$ at LO and $^{+17\%}_{-14\%}$ at NLO for $m_{ZH} = 1$ TeV. We observe a similar pattern for large $p_{T,Z}$, the difference between the OS scheme and the $\overline{\text{MS}}$ with $\mu_t = m_{ZH}$ scheme at $p_{T,Z} \sim 1$ TeV is reduced from a factor of 2.8 at LO to a factor of about 1.9 at NLO.

The K-factor, defined as the ratio of the NLO result in a given scheme to the LO result in the same scheme, is typically larger in the $\overline{\text{MS}}$ scheme than in the OS scheme; this feature is also observed in Higgs pair production [64]. The K-factor of the invariant mass distribution is relatively flat for all scheme choices, with the dynamic scale choices $\mu_t = H_T$

and m_{ZH} yielding $K \sim 2.5 - 2.7$ while the OS scheme has $K \sim 1.6$ for $m_{ZH} \sim 1$ TeV. The $\overline{\text{MS}}$ scheme with $\mu_t = \overline{m}_t(\overline{m}_t)$, where the logarithm appearing in eq. (3.2) vanishes, has a very similar K-factor to the OS scheme; this differs from the HH case where the two schemes had a similar shape but a different normalisation. For the $p_{T,Z}$ distribution the pattern of K-factors for the different schemes is broadly the same as for the invariant mass distribution, but in all cases the K-factors rise with $p_{T,Z}$ reaching up to $K = 5$ for dynamic μ_t choices at $p_{T,Z} = 1$ TeV.

Comparing the results obtained here for $gg \rightarrow ZH$ to other loop-induced processes, such as off-shell Higgs production, Higgs pair production and Higgs plus jet production, we note that the ZH process has a larger mass scheme dependence at LO. For off-shell Higgs production and Higgs pair production going from LO to NLO approximately halves the uncertainty due to the mass scheme choice; in the ZH case we also observe a reduction in the uncertainty, but by less than a factor of 2.

In the HH case, in the high-energy limit, the triangle contribution is suppressed by a factor of $1/s$ w.r.t. the box form factors. Here, the leading high-energy behaviour of the box form factors has the form [63, 70]

$$
\begin{aligned}
A_i^{(0)} &\sim m_t^2 f_i(s,t) \\
A_i^{(1)} &\sim 6 C_F A_i^{(0)} \log\left[\frac{m_t^2}{s}\right] \, ,
\end{aligned}
\tag{3.3}
$$

where the $\log[m_t^2]$ term in $A_i^{(1)}$ is due to the renormalisation of m_t, and the overall power of m_t^2 comes from the Yukawa couplings. Converting to the $\overline{\text{MS}}$ scheme using eq. (3.2) results in a logarithm of the form $\log[\mu_t^2/s]$. In ref. [63] it was argued that choosing $\mu_t^2 \sim s$ minimizes these logarithms and is thus the preferred central scale choice of the Yukawa couplings. However, in the present ZH case, the structure is different. Firstly, the triangle contribution is not suppressed w.r.t. the box form factors, and secondly logarithms involving m_t appear in the box form factors already at leading order. Unlike in the HH case, where the overall power of m_t^2 in eq. (3.3) comes entirely from the top Yukawa couplings, in $gg \rightarrow ZH$ one of the overall m_t factors must come from the top-quark propagators, hence the leading term in the small-mass expansion is already power-suppressed by one power of m_t. Similar, power-suppressed, mass logarithms have been studied in the context of single Higgs production, see for example ref. [71] and references therein. The leading helicity amplitudes for ZH in the high-energy limit have the form

$$
\begin{aligned}
A_i^{(0)} &\sim m_t^2 f_i(s,t) \log^2\left[\frac{m_t^2}{s}\right] \, , \\
A_i^{(1)} &\sim \frac{(C_A - C_F)}{6} A_i^{(0)} \log^2\left[\frac{m_t^2}{s}\right] \, ,
\end{aligned}
\tag{3.4}
$$

Converting to $\overline{\text{MS}}$ generates terms of the form $C_F A^{(0)} \log[\mu_t^2/m_t^2]$, therefore the choice $\mu_t^2 = s$ does not eliminate the leading logarithms involving m_t^2, as is the case for the box form factors of HH.

4 Conclusions

The $gg \to ZH$ channel contributes to the $pp \to ZH$ process starting at NNLO and accounts for around 6% of the total cross section. However, the gluon-fusion channel suffers from a large scale dependence at LO and is a significant source of theoretical uncertainty for Z boson production in association with a Higgs boson at the LHC [1, 2, 12–16].

In this work, we have presented the complete NLO corrections for the loop-induced gluon-fusion channel; they increase the gluon-fusion cross section by about a factor of 2, and reduce the scale dependence. Thus, at N³LO, the gluon induced channel will account for around 10% of the $pp \to ZH$ total cross section. We have investigated the invariant mass distribution and transverse momentum distributions for both the Z boson and Higgs boson. At large transverse momentum, we found that the NLO corrections can be very large, more than 10 times the LO result for $p_{T,H}$; the origin of this behaviour can be traced back to extremely large real radiation corrections when a soft Z boson is radiated from a top quark loop [20]. At NNLO, in the high-p_T region, the gluon fusion channel is suppressed by 1–2 orders of magnitude relative to the dominant $q\bar{q}$ channel. However, due to the large higher-order corrections presented here, we anticipate that at N³LO the gluon-fusion channel will still play a significant role even for $p_T > 500$ GeV.

We have also studied the top quark mass scheme uncertainties for this channel, i.e., the difference between results produced with the top quark mass renormalised in the on-shell scheme and the $\overline{\text{MS}}$ scheme. As for other loop-induced processes with a scale above the top quark pair-production threshold [61–64], we found a large mass scheme uncertainty at LO. At NLO the mass scheme uncertainty is smaller than at LO, but remains at least as large as the usual renormalisation and factorisation scale uncertainties.

The inclusion of the NLO corrections to the gluon-fusion channel is essential for correctly describing ZH production at the LHC and HL-LHC. The size of the NLO corrections, especially for the transverse momentum distributions, and the mass scheme uncertainty motivate a calculation of $gg \to ZH$ beyond NLO and the study of this process beyond fixed order.

Acknowledgments

References

[1] ATLAS collaboration, *Observation of $H \to b\bar{b}$ decays and VH production with the ATLAS detector*, *Phys. Lett. B* **786** (2018) 59 [arXiv:1808.08238] [INSPIRE].

[2] CMS collaboration, *Observation of Higgs boson decay to bottom quarks*, *Phys. Rev. Lett.* **121** (2018) 121801 [arXiv:1808.08242] [INSPIRE].

[3] ATLAS collaboration, *Direct constraint on the Higgs-charm coupling from a search for Higgs boson decays to charm quarks with the ATLAS detector*, Tech. Rep. ATLAS-CONF-2021-021, CERN, Geneva, Switzerland (2021).

[4] CMS collaboration, *Direct search for the Standard Model Higgs boson decaying to a charm quark-antiquark pair*, Tech. Rep. CMS-PAS-HIG-21-008, CERN, Geneva, Switzerland (2022).

[5] L. Altenkamp, S. Dittmaier, R.V. Harlander, H. Rzehak and T.J.E. Zirke, *Gluon-induced Higgs-strahlung at next-to-leading order QCD*, *JHEP* **02** (2013) 078 [arXiv:1211.5015] [INSPIRE].

[6] R.V. Harlander, S. Liebler and T. Zirke, *Higgs strahlung at the Large Hadron Collider in the 2-Higgs-doublet model*, *JHEP* **02** (2014) 023 [arXiv:1307.8122] [INSPIRE].

[7] C. Englert, M. McCullough and M. Spannowsky, *Gluon-initiated associated production boosts Higgs physics*, *Phys. Rev. D* **89** (2014) 013013 [arXiv:1310.4828] [INSPIRE].

[8] W. Bizoń, F. Caola, K. Melnikov and R. Röntsch, *Anomalous couplings in associated VH production with Higgs boson decay to massive b quarks at NNLO in QCD*, *Phys. Rev. D* **105** (2022) 014023 [arXiv:2106.06328] [INSPIRE].

[9] R. Gauld, A. Gehrmann-De Ridder, E.W.N. Glover, A. Huss and I. Majer, *$VH+jet$ production in hadron-hadron collisions up to order α_s^3 in perturbative QCD*, *JHEP* **03** (2022) 008 [arXiv:2110.12992] [INSPIRE].

[10] G. Heinrich, *Collider physics at the precision frontier*, *Phys. Rept.* **922** (2021) 1 [arXiv:2009.00516] [INSPIRE].

[11] ATLAS collaboration, *Measurement of VH, $H \to b\bar{b}$ production as a function of the vector-boson transverse momentum in 13 TeV pp collisions with the ATLAS detector*, *JHEP* **05** (2019) 141 [arXiv:1903.04618] [INSPIRE].

[12] ATLAS collaboration, *Measurement of the associated production of a Higgs boson decaying into b-quarks with a vector boson at high transverse momentum in pp collisions at $\sqrt{s} = 13$ TeV with the ATLAS detector*, *Phys. Lett. B* **816** (2021) 136204 [arXiv:2008.02508] [INSPIRE].

[13] ATLAS collaboration, *Measurements of WH and ZH production in the $H \to b\bar{b}$ decay channel in pp collisions at 13 TeV with the ATLAS detector*, *Eur. Phys. J. C* **81** (2021) 178 [arXiv:2007.02873] [INSPIRE].

[14] ATLAS collaboration, *Combination of measurements of Higgs boson production in association with a W or Z boson in the $b\bar{b}$ decay channel with the ATLAS experiment at $\sqrt{s} = 13$ TeV*, Tech. Rep. ATLAS-CONF-2021-051, CERN, Geneva, Switzerland (2021).

[15] ATLAS collaboration, *Direct constraint on the Higgs-charm coupling from a search for Higgs boson decays into charm quarks with the ATLAS detector*, arXiv:2201.11428 [INSPIRE].

[16] CMS collaboration, *Search for the associated production of the Higgs boson and a vector boson in proton-proton collisions at $\sqrt{s} = 13$ TeV via Higgs boson decays to τ leptons*, *JHEP* **06** (2019) 093 [arXiv:1809.03590] [INSPIRE].

[17] CMS collaboration, *Combined Higgs boson production and decay measurements with up to* $137\,fb^{-1}$ *of proton-proton collision data at* $\sqrt{s} = 13$ *TeV*, Tech. Rep. CMS-PAS-HIG-19-005, CERN, Geneva, Switzerland (2020).

[18] G. Luisoni, P. Nason, C. Oleari and F. Tramontano, $HW^{\pm}/HZ + 0$ *and 1 jet at NLO with the POWHEG BOX interfaced to GoSam and their merging within MiNLO*, *JHEP* **10** (2013) 083 [arXiv:1306.2542] [INSPIRE].

[19] A. Denner, S. Dittmaier, S. Kallweit and A. Mück, *HAWK* 2.0*: a Monte Carlo program for Higgs production in vector-boson fusion and Higgs strahlung at hadron colliders*, *Comput. Phys. Commun.* **195** (2015) 161 [arXiv:1412.5390] [INSPIRE].

[20] B. Hespel, F. Maltoni and E. Vryonidou, *Higgs and Z boson associated production via gluon fusion in the SM and the* 2*HDM*, *JHEP* **06** (2015) 065 [arXiv:1503.01656] [INSPIRE].

[21] D. Goncalves, F. Krauss, S. Kuttimalai and P. Maierhöfer, *Higgs-strahlung: merging the NLO Drell-Yan and loop-induced* $0 + 1$ *jet multiplicities*, *Phys. Rev. D* **92** (2015) 073006 [arXiv:1509.01597] [INSPIRE].

[22] J.M. Campbell, R.K. Ellis and C. Williams, *Associated production of a Higgs boson at NNLO*, *JHEP* **06** (2016) 179 [arXiv:1601.00658] [INSPIRE].

[23] F. Granata, J.M. Lindert, C. Oleari and S. Pozzorini, *NLO QCD+EW predictions for HV and HV +jet production including parton-shower effects*, *JHEP* **09** (2017) 012 [arXiv:1706.03522] [INSPIRE].

[24] W. Astill, W. Bizoń, E. Re and G. Zanderighi, *NNLOPS accurate associated HZ production with* $H \to b\bar{b}$ *decay at NLO*, *JHEP* **11** (2018) 157 [arXiv:1804.08141] [INSPIRE].

[25] A.V. Gritsan, J. Roskes, U. Sarica, M. Schulze, M. Xiao and Y. Zhou, *New features in the JHU generator framework: constraining Higgs boson properties from on-shell and off-shell production*, *Phys. Rev. D* **102** (2020) 056022 [arXiv:2002.09888] [INSPIRE].

[26] B.A. Kniehl, *Associated production of Higgs and Z bosons from gluon fusion in hadron collisions*, *Phys. Rev. D* **42** (1990) 2253 [INSPIRE].

[27] F.F. Freitas, C.K. Khosa and V. Sanz, *Exploring the Standard Model EFT in VH production with machine learning*, *Phys. Rev. D* **100** (2019) 035040 [arXiv:1902.05803] [INSPIRE].

[28] K.-P. Xie and B. Yan, *Probing the electroweak symmetry breaking with Higgs production at the LHC*, *Phys. Lett. B* **820** (2021) 136515 [arXiv:2104.12689] [INSPIRE].

[29] B. Yan and C.P. Yuan, *Anomalous* $Zb\bar{b}$ *couplings: from LEP to LHC*, *Phys. Rev. Lett.* **127** (2021) 051801 [arXiv:2101.06261] [INSPIRE].

[30] L. Chen, G. Heinrich, S.P. Jones, M. Kerner, J. Klappert and J. Schlenk, *ZH production in gluon fusion: two-loop amplitudes with full top quark mass dependence*, *JHEP* **03** (2021) 125 [arXiv:2011.12325] [INSPIRE].

[31] J. Davies, G. Mishima and M. Steinhauser, *Virtual corrections to* $gg \to ZH$ *in the high-energy and large-m_t limits*, *JHEP* **03** (2021) 034 [arXiv:2011.12314] [INSPIRE].

[32] L. Alasfar, G. Degrassi, P.P. Giardino, R. Gröber and M. Vitti, *Virtual corrections to* $gg \to ZH$ *via a transverse momentum expansion*, *JHEP* **05** (2021) 168 [arXiv:2103.06225] [INSPIRE].

[33] L. Bellafronte, G. Degrassi, P.P. Giardino, R. Gröber and M. Vitti, *Gluon fusion production at NLO: merging the transverse momentum and the high-energy expansions*, *JHEP* **07** (2022) 069 [arXiv:2202.12157] [INSPIRE].

[34] G. Wang, X. Xu, Y. Xu and L.L. Yang, *Next-to-leading order corrections for* $gg \to ZH$ *with top quark mass dependence*, *Phys. Lett. B* **829** (2022) 137087 [arXiv:2107.08206] [INSPIRE].

[35] G. Wang, Y. Wang, X. Xu, Y. Xu and L.L. Yang, *Efficient computation of two-loop amplitudes for Higgs boson pair production*, *Phys. Rev. D* **104** (2021) L051901 [arXiv:2010.15649] [ɪɴSPIRE].

[36] A. Hasselhuhn, T. Luthe and M. Steinhauser, *On top quark mass effects to* $gg \to ZH$ *at NLO*, *JHEP* **01** (2017) 073 [arXiv:1611.05881] [ɪɴSPIRE].

[37] J. Davies et al., *Double Higgs boson production at NLO: combining the exact numerical result and high-energy expansion*, *JHEP* **11** (2019) 024 [arXiv:1907.06408] [ɪɴSPIRE].

[38] R.N. Lee, *LiteRed 1.4: a powerful tool for reduction of multiloop integrals*, *J. Phys. Conf. Ser.* **523** (2014) 012059 [arXiv:1310.1145] [ɪɴSPIRE].

[39] A.V. Smirnov and F.S. Chuharev, *FIRE6: Feynman Integral REduction with modular arithmetic*, *Comput. Phys. Commun.* **247** (2020) 106877 [arXiv:1901.07808] [ɪɴSPIRE].

[40] B. Ruijl, T. Ueda and J. Vermaseren, *FORM version 4.2*, arXiv:1707.06453 [ɪɴSPIRE].

[41] L. Chen, *A prescription for projectors to compute helicity amplitudes in D dimensions*, *Eur. Phys. J. C* **81** (2021) 417 [arXiv:1904.00705] [ɪɴSPIRE].

[42] P. Maierhöfer, J. Usovitsch and P. Uwer, *Kira — a Feynman integral reduction program*, *Comput. Phys. Commun.* **230** (2018) 99 [arXiv:1705.05610] [ɪɴSPIRE].

[43] J. Klappert, F. Lange, P. Maierhöfer and J. Usovitsch, *Integral reduction with Kira 2.0 and finite field methods*, *Comput. Phys. Commun.* **266** (2021) 108024 [arXiv:2008.06494] [ɪɴSPIRE].

[44] F. Lange, P. Maierhöfer and J. Usovitsch, *Developments since Kira 2.0*, arXiv:2111.01045 [ɪɴSPIRE].

[45] J. Klappert and F. Lange, *Reconstructing rational functions with FireFly*, *Comput. Phys. Commun.* **247** (2020) 106951 [arXiv:1904.00009] [ɪɴSPIRE].

[46] J. Klappert, S.Y. Klein and F. Lange, *Interpolation of dense and sparse rational functions and other improvements in FireFly*, *Comput. Phys. Commun.* **264** (2021) 107968 [arXiv:2004.01463] [ɪɴSPIRE].

[47] A. von Manteuffel, E. Panzer and R.M. Schabinger, *A quasi-finite basis for multi-loop Feynman integrals*, *JHEP* **02** (2015) 120 [arXiv:1411.7392] [ɪɴSPIRE].

[48] A. von Manteuffel and C. Studerus, *Reduze 2 — distributed Feynman integral reduction*, arXiv:1201.4330 [ɪɴSPIRE].

[49] S. Borowka et al., *pySecDec: a toolbox for the numerical evaluation of multi-scale integrals*, *Comput. Phys. Commun.* **222** (2018) 313 [arXiv:1703.09692] [ɪɴSPIRE].

[50] S. Borowka, G. Heinrich, S. Jahn, S.P. Jones, M. Kerner and J. Schlenk, *A GPU compatible quasi-Monte Carlo integrator interfaced to pySecDec*, *Comput. Phys. Commun.* **240** (2019) 120 [arXiv:1811.11720] [ɪɴSPIRE].

[51] Z. Li, J. Wang, Q.-S. Yan and X. Zhao, *Efficient numerical evaluation of Feynman integrals*, *Chin. Phys. C* **40** (2016) 033103 [arXiv:1508.02512] [ɪɴSPIRE].

[52] G. Heinrich et al., *Expansion by regions with pySecDec*, *Comput. Phys. Commun.* **273** (2022) 108267 [arXiv:2108.10807] [ɪɴSPIRE].

[53] S. Catani and M.H. Seymour, *A general algorithm for calculating jet cross-sections in NLO QCD*, *Nucl. Phys. B* **485** (1997) 291 [*Erratum ibid.* **510** (1998) 503] [hep-ph/9605323] [ɪɴSPIRE].

[54] S. Borowka et al., *Full top quark mass dependence in Higgs boson pair production at NLO*, *JHEP* **10** (2016) 107 [arXiv:1608.04798] [INSPIRE].

[55] G. Cullen et al., *Automated one-loop calculations with GoSam*, *Eur. Phys. J. C* **72** (2012) 1889 [arXiv:1111.2034] [INSPIRE].

[56] G. Cullen et al., *GoSam-2.0: a tool for automated one-loop calculations within the Standard Model and beyond*, *Eur. Phys. J. C* **74** (2014) 3001 [arXiv:1404.7096] [INSPIRE].

[57] S. Borowka et al., *Higgs boson pair production in gluon fusion at next-to-leading order with full top-quark mass dependence*, *Phys. Rev. Lett.* **117** (2016) 012001 [*Erratum ibid.* **117** (2016) 079901] [arXiv:1604.06447] [INSPIRE].

[58] Z. Nagy, *Next-to-leading order calculation of three jet observables in hadron hadron collision*, *Phys. Rev. D* **68** (2003) 094002 [hep-ph/0307268] [INSPIRE].

[59] O. Brein, R. Harlander, M. Wiesemann and T. Zirke, *Top-quark mediated effects in hadronic Higgs-strahlung*, *Eur. Phys. J. C* **72** (2012) 1868 [arXiv:1111.0761] [INSPIRE].

[60] NNPDF collaboration, *Parton distributions from high-precision collider data*, *Eur. Phys. J. C* **77** (2017) 663 [arXiv:1706.00428] [INSPIRE].

[61] S. Amoroso et al., *Les Houches* 2019. *Physics at TeV colliders: Standard Model working group report*, in 11th *Les Houches workshop on physics at TeV colliders: PhysTeV Les Houches*, (2020) [arXiv:2003.01700] [INSPIRE].

[62] J. Baglio, F. Campanario, S. Glaus, M. Mühlleitner, M. Spira and J. Streicher, *Gluon fusion into Higgs pairs at NLO QCD and the top mass scheme*, *Eur. Phys. J. C* **79** (2019) 459 [arXiv:1811.05692] [INSPIRE].

[63] J. Baglio et al., *Higgs-pair production via gluon fusion at hadron colliders: NLO QCD corrections*, *JHEP* **04** (2020) 181 [arXiv:2003.03227] [INSPIRE].

[64] J. Baglio, F. Campanario, S. Glaus, M. Mühlleitner, J. Ronca and M. Spira, *gg → HH: combined uncertainties*, *Phys. Rev. D* **103** (2021) 056002 [arXiv:2008.11626] [INSPIRE].

[65] S. Catani, S. Devoto, M. Grazzini, S. Kallweit and J. Mazzitelli, *Top-quark pair hadroproduction at NNLO: differential predictions with the $\bar{MS}$ mass*, *JHEP* **08** (2020) 027 [arXiv:2005.00557] [INSPIRE].

[66] A. Saibel, S.-O. Moch and M. Aldaya Martin, *Cross-sections for $t\bar{t}H$ production with the top quark $\bar{MS}$ mass*, *Phys. Lett. B* **832** (2022) 137195 [arXiv:2111.12505] [INSPIRE].

[67] S. Alioli et al., *Phenomenology of $t\bar{t}j + X$ production at the LHC*, *JHEP* **05** (2022) 146 [arXiv:2202.07975] [INSPIRE].

[68] K.G. Chetyrkin, J.H. Kühn and M. Steinhauser, *RunDec: a Mathematica package for running and decoupling of the strong coupling and quark masses*, *Comput. Phys. Commun.* **133** (2000) 43 [hep-ph/0004189] [INSPIRE].

[69] F. Herren and M. Steinhauser, *Version 3 of RunDec and CRunDec*, *Comput. Phys. Commun.* **224** (2018) 333 [arXiv:1703.03751] [INSPIRE].

[70] J. Davies, G. Mishima, M. Steinhauser and D. Wellmann, *Double Higgs boson production at NLO in the high-energy limit: complete analytic results*, *JHEP* **01** (2019) 176 [arXiv:1811.05489] [INSPIRE].

[71] T. Liu, S. Modi and A.A. Penin, *Higgs boson production and quark scattering amplitudes at high energy through the next-to-next-to-leading power in quark mass*, *JHEP* **02** (2022) 170 [arXiv:2111.01820] [INSPIRE].